

# Mechanical and shape memory properties of porous Ni<sub>50.1</sub>Ti<sub>49.9</sub> alloys manufactured by selective laser melting



Mohsen Taheri Andani<sup>a,b</sup>, Soheil Saedi<sup>c</sup>, Ali Sadi Turabi<sup>c</sup>, M.R. Karamooz<sup>d</sup>,  
Christoph Haberland<sup>a</sup>, Haluk Ersin Karaca<sup>c</sup>, Mohammad Elahinia<sup>a,\*</sup>

<sup>a</sup> Dynamic and Smart Systems Laboratory, Mechanical Industrial and Manufacturing Engineering Department, The University of Toledo, 2801 W Bancroft St. MS 312 Toledo, OH 43606, USA

<sup>b</sup> SM. Wu Manufacturing Research Center, College of Engineering, Department of Mechanical Engineering, University of Michigan, Ann Arbor, MI 48109, USA

<sup>c</sup> Department of Mechanical Engineering, University of Kentucky, Lexington, KY 40506-0503, USA

<sup>d</sup> Department of Mechanical Engineering, Graduate University of Advanced Technology, 76311-33131, Kerman, Iran

## ARTICLE INFO

### Keywords:

Shape memory alloy  
Porous implant  
Stress shielding  
NiTi  
Additive manufacturing  
Selective laser melting  
Plastic strain  
Cyclic test of NiTi

## ABSTRACT

Near equiatomic NiTi shape memory alloys were fabricated in dense and designed porous forms by Selective Laser Melting (SLM) and their mechanical and shape memory properties were systematically characterized. Particularly, the effects of pore morphology on their mechanical responses were investigated. Dense and porous NiTi alloys exhibited good shape memory effect with a recoverable strain of about 5% and functional stability after eight cycles of compression. The stiffness and residual plastic strain of porous NiTi were found to depend highly on the pore shape and the level of porosity. Since porous NiTi structures have lower elastic modulus and density than dense NiTi with still good shape memory properties, they are promising materials for lightweight structures, energy absorbers, and biomedical implants.

## 1. Introduction

Nickel Titanium (NiTi) shape memory alloys exhibit shape memory effect (SME) and superelasticity (SE), and have excellent erosion (Shida and Sugimoto, 1991), corrosion (Oshida Yoshiki, 1991), and wear resistance (Li, 1996; Lin et al., 1997). Consequently, NiTi has been employed in aerospace, automotive, and oil industries (Melton and Duerig, 1985; Hartl and Lagoudas, 2007). In addition, thanks to their good biocompatibility (Ryhänen et al., 1997; Berger-Gorbet et al., 1996; Assad et al., 1993) and mechanical properties, NiTi alloys are remarkable materials for dental and biomedical applications such as stents and orthodontic arch wires (Itin et al., 1994; Kang et al., 2002). However, manufacturing and processing of NiTi alloys are quite challenging (Elahinia et al., 2012). Machining of NiTi results in low-quality work piece along with tool wear due to induced work hardening and spring back effects (Andani et al., 2014a, 2014b). Conventional high-temperature processing methods such as melting and casting could result in increasing the impurity levels and thus, low functional NiTi components (Chen, 1999; Wu, 2002). Furthermore, conventional manufacturing processing does not allow for the production and

engineering of porous NiTi (Andani et al., 2014a, 2014b). Recently, Additive Manufacturing (AM) has offered unique opportunity to overcome the manufacturing difficulties in producing NiTi samples (Haberland et al., 2012, 2013, 2014; Walker et al., 2013; Khoo et al., 2015; Andani et al., 2014a, 2014b; Walker et al., 2014; Esfahani et al., 2016; Elahinia et al., 2016; Taheri Andani, 2015; Ravari et al., 2016; Leist and Zhou, 2016; Dadbakhsh et al., 2014, 2016; Krishna et al., 2009; Bimber et al., 2016; Taheri Andani, 2015). AM builds up a material directly from CAD data in layer by layer or even pixel by pixel to the desired shape (Wu et al., 2015; Cai et al., 2015). Consequently, complex components such as lattice-like structures can be fabricated with ease. Fabricated parts by using selective laser melting (SLM) technology show low impurity, microstructure control and meet the requirements prescribed in the ASTM F2063-05 for medical NiTi-devices (Meier et al., 2009; Haberland, 2012; Bormann et al., 2014). Furthermore, SLM facilitated the fabrication of application specific and engineered porous NiTi structures (Saedi et al., 2016).

Porous NiTi structures have lower elastic modulus than that of the bulk NiTi and their mechanical properties can be tailored by designing the pore size, shape, and distribution (Bernard et al., 2012). One of the

\* Corresponding author.

E-mail addresses: [mtaheri@umich.edu](mailto:mtaheri@umich.edu) (M. Taheri Andani), [soheil.saedi@uky.edu](mailto:soheil.saedi@uky.edu) (S. Saedi), [sadi.turabi@uky.edu](mailto:sadi.turabi@uky.edu) (A.S. Turabi), [m.karamooz@kgut.ac.ir](mailto:m.karamooz@kgut.ac.ir) (M.R. Karamooz), [haberlandchristoph@gmail.com](mailto:haberlandchristoph@gmail.com) (C. Haberland), [karacahaluk@uky.edu](mailto:karacahaluk@uky.edu) (H.E. Karaca), [mohammad.elahinia@utoledo.edu](mailto:mohammad.elahinia@utoledo.edu) (M. Elahinia).

<http://dx.doi.org/10.1016/j.jmbbm.2017.01.047>

Received 26 July 2016; Received in revised form 3 January 2017; Accepted 28 January 2017

Available online 31 January 2017

1751-6161/ © 2017 Elsevier Ltd. All rights reserved.

most promising applications for porous NiTi is bone implant since NiTi exhibit hysteretic behavior during stress cycling similar to the bone (Morgan, 2004). The porosity of 50–80%, together with the super-elastic properties of NiTi can decrease the risk of stress shielding effect and could make a better match to the elastic modulus of natural bone (Krishna et al., 2007; Shishkovsky et al., 2008; Köhl et al., 2007; Imwinkelried, 2007). Furthermore, pore size, geometry, and connectivity result in greater permeability that allows blood vessels migrate, enable bone in-growth, and improves the strength of the implant/bone interconnection (Kang et al., 2002; Simske et al., 1997; Urban et al., 1996; Kienapfel et al., 1999; Yavari et al., 2014; Ahmadi et al., 2014). However, it should be noted that SLM parameters affect the phase transformation temperatures, thermo-mechanical behavior, micro-structure, texture, and the grain size of the fabricated parts (Dadbakhsh et al., 2016, 2014, 2015; Bormann et al., 2014; Hamilton et al., 2015). The possibility of controlling the shape memory response through SLM parameters opens a promising window for manufacturing of NiTi components.

In this work, cellular lattice structured NiTi samples with selected morphology and levels of porosity were fabricated via SLM method. The mechanical properties and shape memory response of the porous SLM fabricated Ni<sub>50.1</sub>Ti<sub>49.9</sub> (atomic %) parts were investigated and compared to that of the dense sample. Furthermore, since a bone implant may experience several cyclic loading during its operation causing the accumulation of plastic strain, functional stability along with the effects of cyclic loading on the mechanical response of NiTi cellular lattice structures are also assessed.

## 2. Fabrication

Porous NiTi parts are generated by repeating identical unit cells in  $x$ ,  $y$ , and  $z$  directions. In this study, three different geometries are selected as unit cells. The first unit cell consists of three orthogonal struts that intersect at the midpoint as shown in Fig. 1(a) and this type is named as a simple cubic (SC) unit cell in this paper. The second unit cell is named as BCC which is constructed by eight diagonal struts to connect the center of the upper and lower faces of a cube to the center of its vertical edges as shown in Fig. 1(b). The third unit cell is named as BCC-Z and it has an additional vertical strut than the BCC, which connects the center of the lower and upper faces as shown in Fig. 1(c). The lattice structures created from BCC and BCC-Z unit cells offer nearly optimized configurations for bending, compression, and shear loadings (Ravari et al., 2016, 2014; Ravari and Kadkhodaei, 2015).

To investigate the mechanical properties of the above-mentioned cellular lattices, three different parameters should be defined; strut diameter (D), cell length (L), and the number of repeating unit cells along each direction. Table 1 shows the selected parameters along with the relevant level of porosity which is defined as the ratio of the pore volumes (include the closed pores within the struts) to the total volume of the solid part. The level of porosities is selected based on our previous study on achieving biocompatible stiffness in NiTi through additive manufacturing (Andani et al., 2016).

**Table 1**

The dimensions of specimens and their relative level of porosity.

Name	D (mm)	L (mm)	Number of Cells	Porosity (%)
Dense	4.78	10	–	0
SC-32	1.4	2	4 × 4 × 4	32
SC-45	1.2	2	4 × 4 × 4	45
SC-58	1	2	4 × 4 × 4	58
BCC-Z	0.65	2.33	4 × 4 × 3	65
BCC	0.65	2.33	4 × 4 × 3	69

The sample dimensions used for fabrication of porous SC and BCC/BCC-Z for mechanical tests were 8×8×8 mm<sup>3</sup> and 9.32×9.32×7 mm<sup>3</sup>, respectively. Two plates were attached to the bottom and top of each cell to facilitate the uniaxial compression testing. The thicknesses of these plates were 1.5 mm and 0.93 mm for SC and BCC/BCC-Z, respectively. Optical images of porous samples are shown in Fig. 2.

Phenix-PXM selective laser melting machine (3D Systems, Rock Hill, SC) was used for SLM fabrication. The machine was equipped with a 300 W Ytterbium fiber laser (CW,  $\lambda=1070$  nm, TEM00). A tungsten roller distributed a layer of powder onto a build platform. The beam was focused by a system of galvanometric mirrors and create a beam diameter of approximately 80  $\mu$ m at the focal point. The powder particles became fully molten upon absorption of laser radiation and then bound to each other to make an entirely dense layer after re-solidification. The build platform was then lowered, and the next layer of NiTi powder was deposited on top. By repeating this process, the parts were built up layer by layer in the powder bed.

Ni<sub>50.1</sub>-Ti<sub>49.9</sub>(at%) ingot (Nitinol Devices & Components, Inc. Fremont, CA) was atomized by TLS Technik GmbH (Bitterfeld Germany) using Electrode Induction-melting Gas Atomization (EIGA) method. Then, the resulting powder was sieved to 25–75  $\mu$ m particle size. For the current study to make dense parts from NiTi powder, the effective laser powder, layer thickness, scanning velocity, and hatch distance were selected to be 250 W, 30 mm, 1.25 m/s, and 120  $\mu$ m, respectively. They have been selected based on our previous study on part density, impurity pickup, transformation characteristics, and functional behavior of SLM fabricated NiTi alloys (Walker et al., 2016).

A Perkin-Elmer DSC Pyris 1 was used to determine the transformation temperatures (TTs), and the heating/cooling rate was 10 °C/min in a nitrogen atmosphere. Compression tests were conducted by 100kN MTS Landmark servo-hydraulic test platform. A strain rate of 10<sup>-4</sup> s<sup>-1</sup> was employed during loading and unloading was performed at a rate of 100 N/sec under force control. An attached high-temperature extensometer to grips measured the strain. Heating of the specimens occurred by using mica band heaters retrofitted to the compression grips and cooling was achieved through internal liquid nitrogen flow in the compression grips. K-type thermocouples measured the temperature and controlled by using Omega CN8200 Series temperature controller. The heating rate of 10 °C/min and a cooling rate of 5 °C/min were applied.

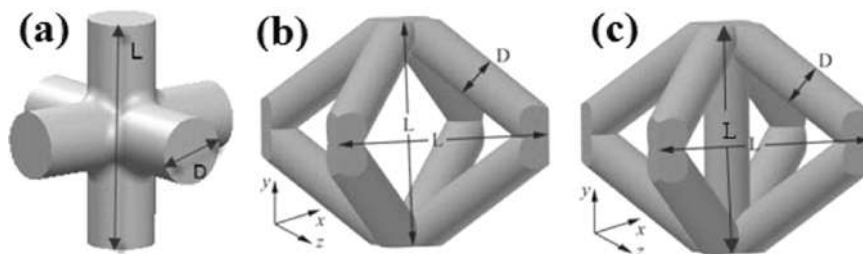


**Fig. 1.** The repeating unit cell of a) SC, b) BCC and c) BCC-Z cellular lattice structure.

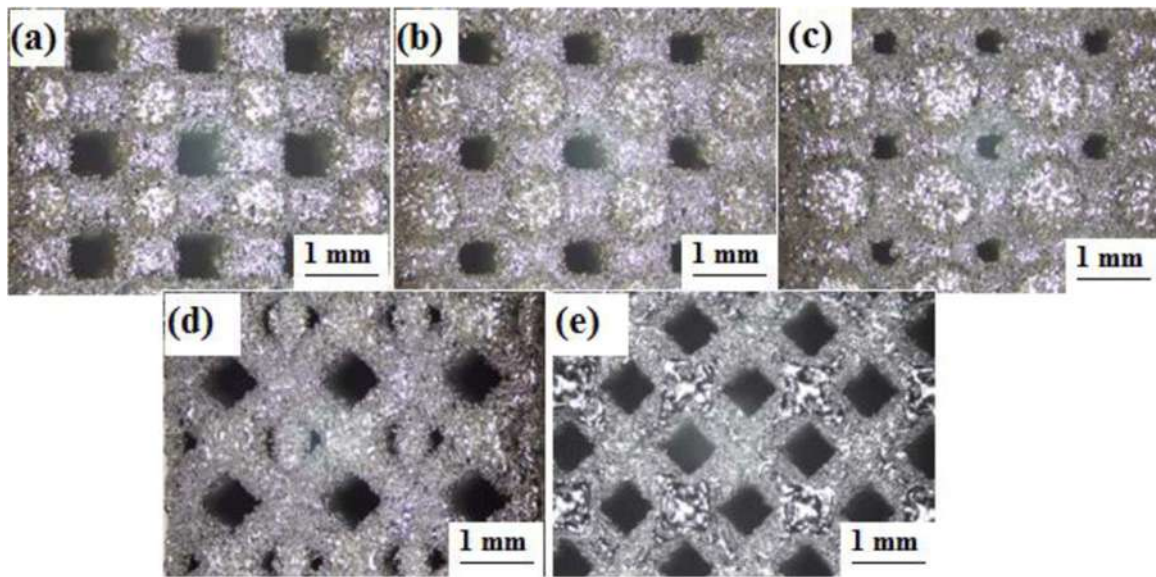


Fig. 2. Images of SLM fabricated NiTi parts. (a) SC-58, (b) SC-45, (c) SC-32, (d) BCC-Z, and (e) BCC.

### 3. Results and discussion

#### 3.1. Phase transformation reponses

Fig. 3 shows the DSC plots of the initial ingot, powder, and SLM  $Ni_{50.1}Ti_{49.9}$ . Multiple peaks were observed for powder DSC which was attributed to the inhomogeneous heat transfer in the powder and/or compositional inhomogeneity of particles (Saedi et al., 2016). While the initial ingot showed a small shoulder during martensitic transformation, phase transformation of SLM fabricated sample occurred in a single peak. Temperature hysteresis of the ingot and SLM samples were almost the same. However, TTs were different. TTs determined from the DSC results are shown in Table 2. TTs had slightly shifted to lower temperatures after powder atomization, and then they increased after SLM process. When compared to the ingot, in the SLM sample,  $M_s$  and  $M_f$  were decreased by 15 °C and 13 °C while  $A_s$  and  $A_f$  were decreased by about 10 °C and 15 °C, respectively. The change in TTs after SLM process can be attributed to the picked up impurities, particularly oxygen and carbon during the process. Since titanium is active, secondary phases such as TiC, TiO<sub>2</sub>, Ti<sub>2</sub>NiO<sub>x</sub> can be formed. The formation of such Ti-rich secondary phases increases the Ni concentration of the matrix as well as they may hinder the martensite nucleation and consequently decreases the TTs (Frenzel et al., 2007).

Fig. 4 shows the DSC curves of ingot and SLM  $Ni_{50.1}Ti_{49.9}$  for 20 cycles. For both samples, TTs decreased and then stabilized with

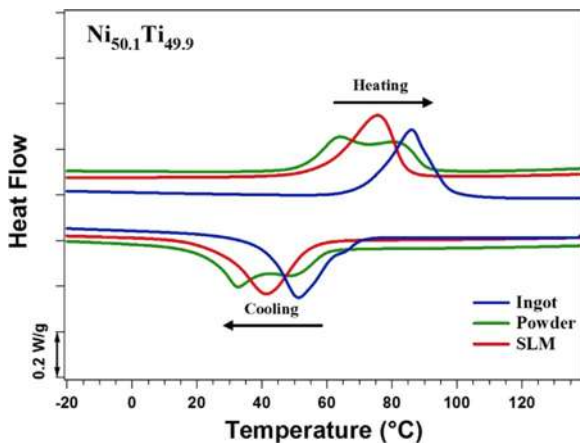


Fig. 3. DSC plots of equiatomic Powder and SLM NiTi and Ingot.

Table 2

Transformation temperatures of equiatomic Ingot, Powder, and SLM NiTi extracted from DSC plots.

$Ni_{50.1}Ti_{49.9}$	$M_s$ (°C)	$M_f$ (°C)	$A_s$ (°C)	$A_f$ (°C)
Ingot	73	39	69	100
Powder	59	23	53	91
SLM	58	26	59	85

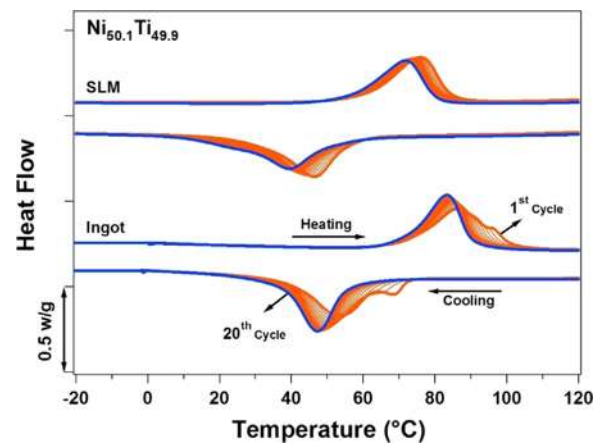


Fig. 4. Thermal cycling behavior of ingot and SLM  $Ni_{50.1}Ti_{49.9}$ .

thermal cycling. The  $A_f$  and  $M_s$  temperatures of the initial ingot decreased from 100 °C and 73 °C at first cycle to 91 °C and 56 °C at the 20th cycle. The  $A_f$  and  $M_s$  temperatures of the SLM fabricated sample dropped from 85 °C and 58 °C at first cycle to 80 °C and 52 °C at the 20th cycle. The shift of TTs to lower temperatures is in good agreement with literature (Wagner et al., 2006; Karaca et al., 2013). Thermal cycling results in increased dislocation density and statistically distributed martensite variants results in opposing strain fields. These fields accommodate on each other or slow down the growth of new martensite. Therefore,  $M_s$  decreases steadily during cycling. With increasing the cycling number, smaller martensite plates form between the larger regions of stabilized martensite. This results in a higher number of martensite/austenite interfaces and consequently increases a driving force for reverse transformation upon heating and therefore the  $A_s$  also decreases (Wagner et al., 2006). Similar results for near

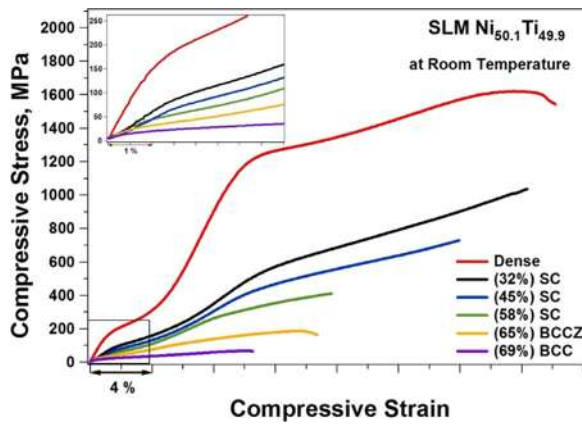


Fig. 5. Compressive response of dense and porous SLM  $\text{Ni}_{50.1}\text{Ti}_{49.9}$  samples at room temperature.

equiatomic NiTi produced by SLM are reported in previous works (Meier et al., 2009; Haberland, 2012).

### 3.2. Stress strain response

Fig. 5 compares the compressive response of dense and porous samples up to failure at 24 °C. It is clear that the mechanical response of NiTi is highly affected by adding porosity to the structures. Young modulus, critical stresses, and strains were all decreased with increased porosity level which is in good agreement with our previous study (Andani et al., 2016; Haberland et al., 2013). Ductility of the samples was also decreased with porosity. While dense structure endured the deformation of 30.2% and failed at 1620 MPa, SC-58 was failed after 15.6% at 410 MPa. BCC-69 was failed at 63 MPa with 10.5% deformation. Pore morphology also affects the mechanical response of the samples. It has been previously shown that by increasing the portion of the axial load in the deformation mechanisms of a porous material, the stiffness of that material would increase in the loading direction. However, in the case of porous SMAs, by increasing the portion of bending in the deformation mechanisms of a porous SMA, the effects of asymmetric material response will increase (Ravari et al., 2016).

Fig. 6a shows the temperature dependent compressive response of the dense sample. The first test was conducted at 80 °C which is above  $M_s$ . The sample was loaded up to 5% strain where stress-induced martensite transformation was observed and then unloaded. Superelasticity is not observed since the testing temperature is below  $A_f$ , however when the sample was heated above  $A_f$ , recoverable strain ( $\epsilon_{rec}$ ) of 2.9% was observed due to back transformation. The irrecoverable strain ( $\epsilon_{irr}$ ) was 0.85% after heating, which can be attributed to

plastic deformation and/or stabilized martensite. The testing temperature was increased by 20 °C at the next step and the same procedure repeated. At 100 °C and 120 °C, partial recovery was observed during unloading and further recovery was observed during heating. At 100 °C, the  $\epsilon_{rec}$  was 2.5% upon unloading and 4.1% after heating. At 120 °C, the  $\epsilon_{rec}$  was increased to 3.1% upon unloading and further recovery was not observed upon heating. The superelastic recovery was decreased at 140 °C since increased temperature results in the higher required critical stress for martensitic transformation and thus, increased plastic deformation. Based on the above results, 120 °C was chosen to run superelastic cycling tests as shown in Fig. 6b. The samples were cycled eight times between 5 and 800 MPa. In the first cycle, the sample is loaded till 8% and only small back transformation was observed upon unloading with  $\epsilon_{irr}$  of 5%. The response is stabilized with cycling and stress hysteresis and  $\epsilon_{irr}$  of each cycle were decreased with increasing number of cycles. At the eight cycle, the  $\epsilon_{irr}$  was less than 0.1% and the total residual strain in the sample was determined to be 6%.

The poor superelastic response of the SLM fabricated NiTi samples is as expected since equiatomic NiTi do not show superelasticity even in the solutionized conditions due to low strength (Funakubo and Kennedy, 1987). One of the practical methods to improve the shape memory properties of NiTi alloys is the use of Ni-rich alloys and precipitation (Saedi et al., 2016). Another advantage of Ni-rich samples is their lower transformation temperatures. Additionally, SLM fabricated samples are prone to formation of secondary phases inner defects such as pores, unmolten particles or internal cracks which can affect the strength of material in compared to conventionally fabricated NiTi (Saedi et al., 2016; Kasperovich and Hausmann, 2015; Saedi et al., 2016).

NiTi cellular lattice structures are suitable candidates to be used as bone implants. A bone implant may experience several cyclic loading during its operation which results in the accumulation of plastic strain. To assess the effects of cyclic loading on the mechanical response of NiTi cellular lattice structures, all the fabricated samples tested under stress-controlled cyclic compression. Fig. 7 shows the cyclic mechanical behavior of dense and SC porous samples to evaluate the functional stability of the shape memory effect. In each cycle, the sample was deformed at room temperature in martensite state and the plateau corresponds to detwinning of martensite. After reaching to certain stress level, the sample was unloaded and heated up to 140 °C, which is well above  $A_f$  and then cooled back to room temperature for next cycle. The procedure was repeated for eight times. The maximum stress level for each sample was determined according to the failure results provided in Fig. 4. It is well known that equiatomic NiTi alloys have poor superelastic responses due to their low strength (Funakubo and Kennedy, 1987). Thus, in general, they are used in applications where shape memory effect is employed.

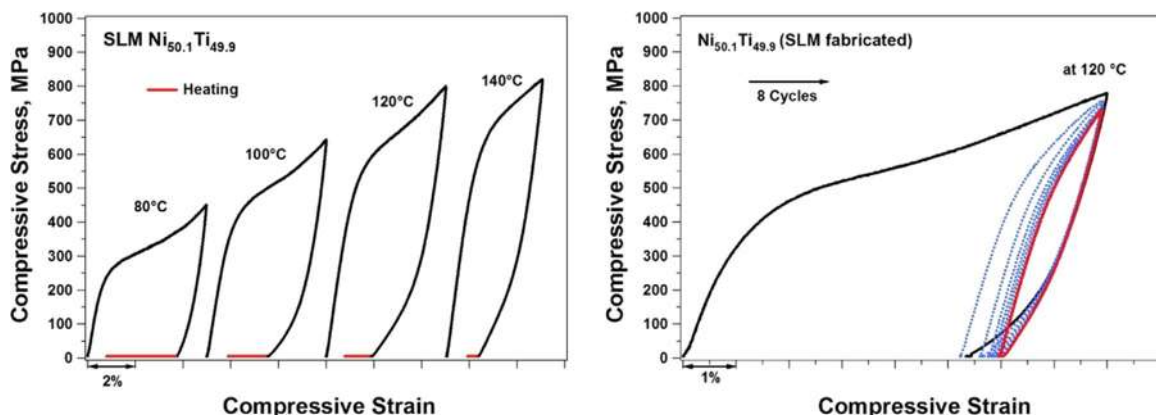


Fig. 6. a. Temperature dependent stress-strain curves and b. Superelasticity cycling of dense SLM  $\text{Ni}_{50.1}\text{Ti}_{49.9}$  sample.

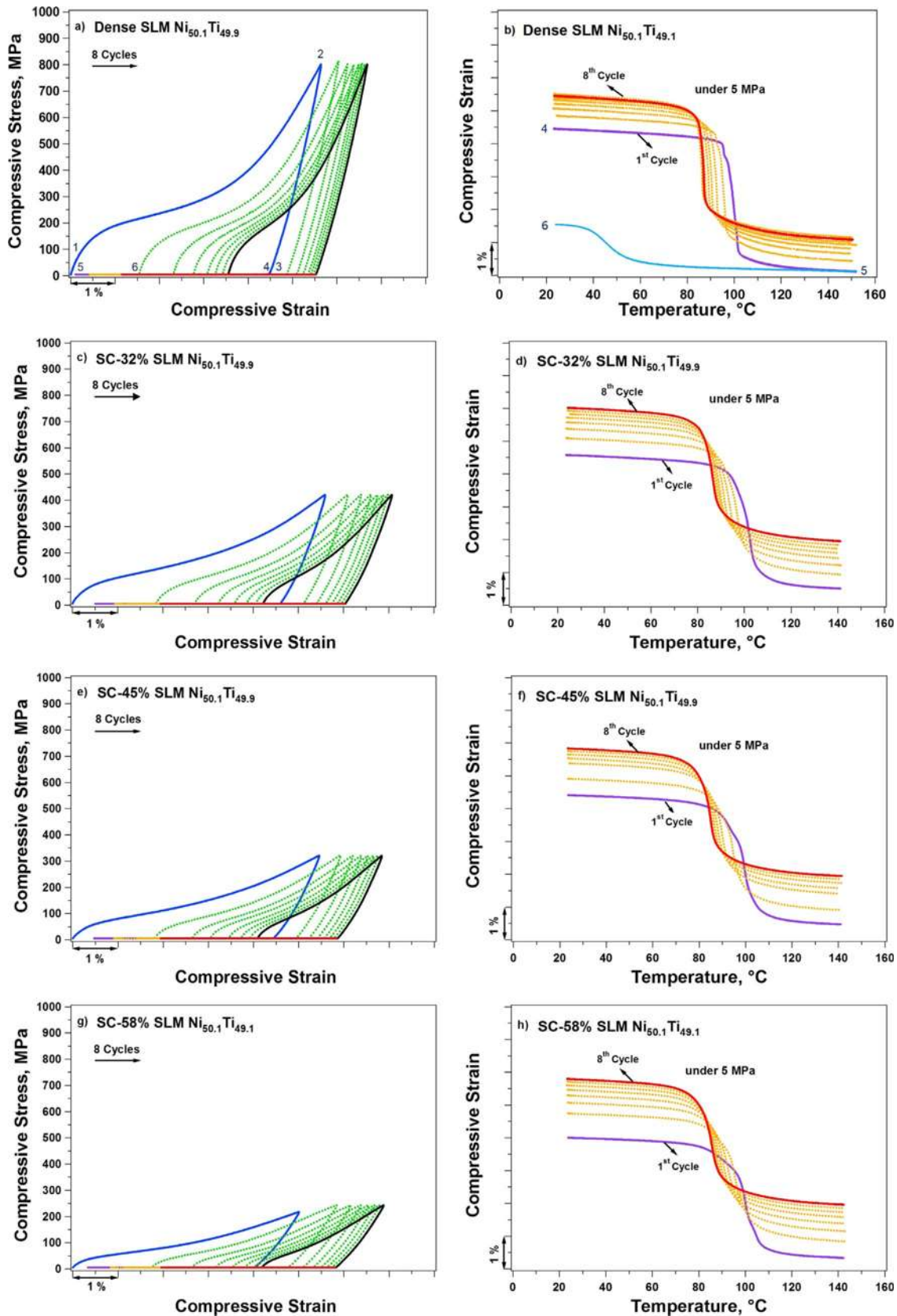


Fig. 7. a, c, e, g Stress-strain curves of cycling tests of Dense, SC-32, SC-45 and SC-58 SLM Ni<sub>50.1</sub>Ti<sub>49.9</sub>, b, d, f, h The heating procedure of the same experiment to above A<sub>f</sub> after unloading.

Fig. 7a displays the stress-strain responses of the dense sample at room temperature while 7b shows the strain recovery curves of the samples upon heating. To comprehend the figures, the test procedure for the first cycle has been sequenced. First, samples were loaded at

room temperature to selected stress level (process 1–2) and then unloaded (process 2–3) to 5 MPa. Next, the samples were heated up to a temperature above A<sub>f</sub> temperature (process 3–4) to observe the recovery. Lastly samples were cooled down to room temperature to

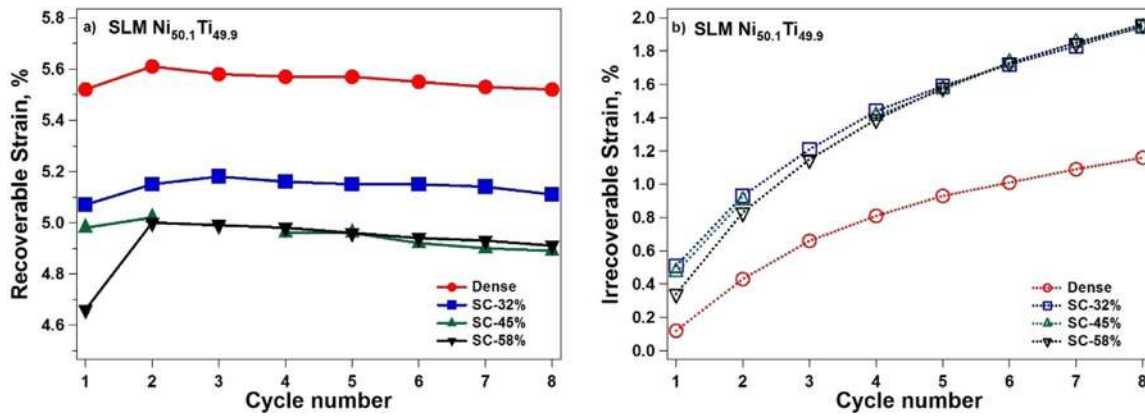


Fig. 8. The change of a.  $\epsilon_{rec}$  and b.  $\epsilon_{irr}$  with cycling the of dense, SC-58, SC-45 and SC-32 samples.

start the next cycle (process 5–6). Due to the back transformation and induced strain upon cooling, the second cycle starts at point 6. The process 5–6 were omitted for the rest of cycles to make the figure clear. Applied maximum stresses during the cycling tests were 800 MPa for the dense sample. Stress levels of 420, 320, and 240 MPa were used for SC-32, SC-45, and SC-58 porous samples, respectively, which were adjusted due to their density. Dense sample shows full shape recovery upon heating at first cycle while negligible irrecoverable strain was observed in porous samples, however, all as the number of cycles were increased the response was stabilized and full recovery was achieved in all of the samples. Fig. 8a and b depict the evolution of  $\epsilon_{rec}$  and  $\epsilon_{irr}$ , respectively, with cycling where the data were extracted from Fig. 7. An accumulation of  $\epsilon_{irr}$  occurs during cycling. The highest  $\epsilon_{irr}$  can be observed in the first cycle, while they decay by increasing cycles. Moreover, the amount of  $\epsilon_{irr}$  increases by increasing the level of porosity.

Fig. 9 shows the shape memory effect of BCC and BCC-Z porous samples. According to the failure tests, the maximum stress levels for cycling experiments of BCC and BCC-Z were determined. Consequently, BCC-Z and BCC loaded up to 90 and 50 MPa at 24 °C respectively. After unloading to 5 MPa, the samples were heated above  $A_f$  to observe shape recovery and cooled back to room temperature for next cycle. In the first cycle, the samples were deformed till 3.8 and 4.8% for BCC-Z and BCC, respectively, and fully recovered upon unloading and subsequent heating. The strain curves during heating show that the transformation temperatures slightly reduced in the second cycle. It should be noted that the maximum applied stresses are very low in BCC and BCC-Z structures due to their higher porosity levels than SC samples.

The maximum residual strain of all samples was decreased with cycling. Because of the porous microstructure of the samples, some portions of the sample may experience higher plastic deformation than

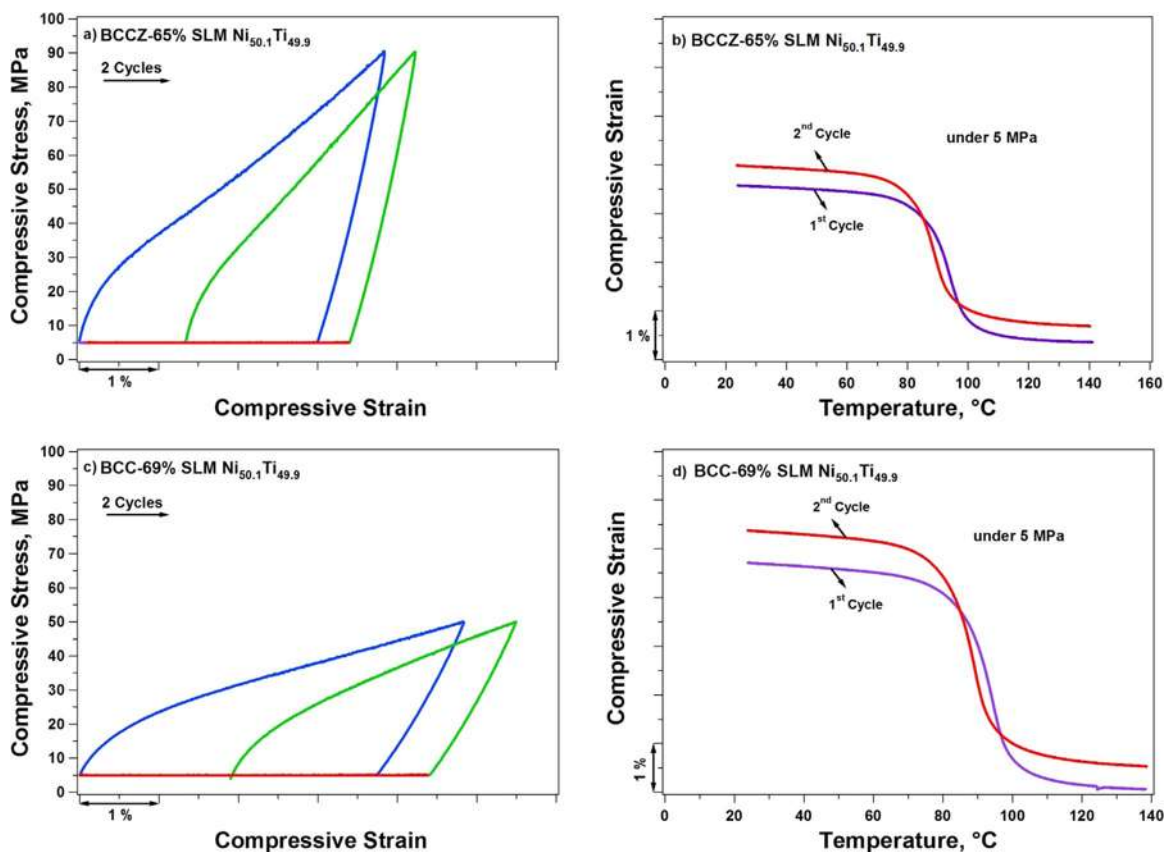


Fig. 9. a, c. Stress-strain curves for cycling tests and b, d. The heating procedure of the same experiment to above  $A_f$  after unloading to 5 MPa. of BCC and BCC-Z.

**Table 3**Summary of stress-strain curves of cycling tests of Dense, 58%, 45%, 32% porosity. BCC and BCC-Z SLM Ni<sub>50.1</sub>Ti<sub>49.9</sub>.

SLM Ni <sub>50.1</sub> Ti <sub>49.9</sub>	Elastic Modulus, (GPa)	Ultimate Comp. Stress, (MPa)	Failure Strain, %	Max Stress Level for cycling, (MPa)	1st Cycle			Last Cycle	
					Irrec. Strain, %	Rec. Strain, %	Recovery Ratio, %	Rec. Strain, %	Total Irrec. Strain, %
Dense	69.0	1619	30.2	800	0.12	5.52	97.8	5.52	1.16
SC-32	41.2	1035	28.3	420	0.51	5.07	90.8	5.11	1.95
SC-45	30.0	728	24	320	0.47	4.98	91.3	4.89	1.94
SC-58	20.5	410	15.6	240	0.34	4.66	93.2	4.91	1.96
BCC-Z	16.5	187	13.6	90	0	3.4	100	3.3	0

others due to stress concentrations. The increased slope during transformation in BCC and BCC-Z samples in comparison with SC structure can be attributed to increased plastic deformation due to variant-variant interaction and dissipation. The slope of transformation strongly depends on the pore morphology, microstructural defects, and martensite morphology.

Elastic modulus, ultimate compressive stress, failure strain, maximum applied stress,  $\epsilon_{rec}$ , and  $\epsilon_{irr}$  in the first cycle,  $\epsilon_{rec}$  in the eight cycle, and total irrecoverable strain ( $\epsilon_{irr,tot}$ ) are summarized in Table 3. The recovery ratio at first cycle was calculated as the ratio of recoverable strain to total strain.

The dense sample exhibited the highest  $\epsilon_{rec}$  of 5.52% and lowest  $\epsilon_{irr}$  of 1.16% after eight cycles. SC-32 displayed  $\epsilon_{rec}$  of 5.07% and  $\epsilon_{irr}$  of 0.5% in the first cycle. When porosity increased to 58%, the  $\epsilon_{rec}$  was 4.66% and  $\epsilon_{irr}$  was 0.34% in the first cycle. All the porous SC samples and dense part showed more than 90% recovery in the first cycle and accumulation of  $\epsilon_{irr}$  during cycling. There is a considerable increase in the  $\epsilon_{rec}$  in the second cycle for dense and all porous SC sample. After this cycle the  $\epsilon_{rec}$  is leveled and then declined with increased cycle number (Fig. 8a). After cycling, all porous samples showed stabilized shape memory effect with recoverable strain of 5%.

The dense sample has the highest elastic modulus of 69 GPa, and the modulus decreased by increasing the level of porosity.

#### 4. Conclusion

Selective laser melting was used to produce dense and porous near equiatomic NiTi parts, and thermo-mechanical tests were conducted to characterize the mechanical and shape memory properties. In addition to the dense sample, five porous samples with a different level of porosity from 32% to 69% with two different structures were characterized. Transformation temperatures decreased slightly (about 10–14 °C) after SLM, which was attributed to composition change and picked up impurities. The superelastic response of the SLM fabricated near equiatomic NiTi showed only partial recovery. This fact is attributed to the low strength of equiatomic NiTi. The dense and porous samples showed good shape memory effect and functional stability. Dense SLM NiTi recovered almost entirely while less than 0.5% irrecoverable strain remained in porous samples. At the end of cycling tests, SME behavior stabilized, and their irrecoverable strain was negligible.

Mechanical properties of samples such as elastic modulus and ductility of the SLM fabricated NiTi samples found to be highly porosity level and pore structure dependent. It was shown that it is feasible to decrease the elastic modulus of the samples up to 86% by increased porosity and still retain the shape memory effect of SLM fabricated samples.

#### Acknowledgements

The authors acknowledge funding from the US State of Ohio Department of Development through Grant WP10-010 (Nitinol Commercialization Accelerator), TVSF Grant TECG2014095 (Ankle

Foot Orthosis Using Shape Memory Alloys) and NASA EPSCOR Program under Grant no.: NNX11AQ31A.

#### References

- Ahmadi, S., et al., 2014. Mechanical behavior of regular open-cell porous biomaterials made of diamond lattice unit cells. *J. Mech. Behav. Biomed. Mater.* 34, 106–115.
- Andani, M.T., et al., 2014a. Metals for bone implants. Part 1. Powder metallurgy and implant rendering. *Acta Biomater.* 10 (10), 4058–4070.
- Andani, M.T., et al., 2014b. An investigation of effective process parameters on phase transformation temperature of nitinol manufactured by selective laser melting. In: Proceedings of the ASME 2014 Conference on Smart Materials, Adaptive Structures and Intelligent Systems. American Society of Mechanical Engineers.
- Andani, M.T., et al., 2016. Achieving biocompatible stiffness in NiTi through additive manufacturing. *J. Intell. Mater. Syst. Struct.*, [1045389X16641199].
- Assad, M., et al., Assays of cytotoxicity of the Nickel-Titanium shape memory alloy. In: *Annales de chirurgie*. 1993.
- Berger-Gorbet, M., et al., 1996. Biocompatibility testing of NiTi screws using immunohistochemistry on sections containing metallic implants. *J. Biomed. Mater. Res.* 32 (2), 243–248.
- Bernard, S., et al., 2012. Compression fatigue behavior of laser processed porous NiTi alloy. *J. Mech. Behav. Biomed. Mater.* 13, 62–68.
- Bimber, B.A., et al., 2016. Anisotropic microstructure and superelasticity of additive manufactured NiTi alloy bulk builds using laser directed energy deposition. *Mater. Sci. Eng.: A* 674, 125–134.
- Bormann, T., et al., 2014. Microstructure of selective laser melted nickel–titanium. *Mater. Charact.* 94, 189–202.
- Cai, X., et al., 2015. Measurement and characterization of porosity in aluminium selective laser melting parts using X-ray CT. *Virtual Phys. Prototyp.* 10 (4), 195–206.
- Chen, C., 1999. A study on the machinability of a Ti49.6Ni50.4 shape memory alloy. *Mater. Lett.* 40, 27–32.
- Dadbakhsh, S., et al., 2014. Effect of SLM parameters on transformation temperatures of shape memory nickel titanium parts. *Adv. Eng. Mater.* 16 (9), 1140–1146.
- Dadbakhsh, S., et al., 2015. Influence of SLM on shape memory and compression behaviour of NiTi scaffolds. *CIRP Ann.-Manuf. Technol.* 64 (1), 209–212.
- Dadbakhsh, S., et al., 2016. Texture and anisotropy in selective laser melting of NiTi alloy. *Mater. Sci. Eng.: A* 650, 225–232.
- Elahinia, M., et al., 2016. Fabrication of NiTi through additive manufacturing: a review. *Progress. Mater. Sci.* 83, 630–663.
- Elahinia, M.H., et al., 2012. Manufacturing and processing of NiTi implants: a review. *Progress. Mater. Sci.* 57 (5), 911–946.
- Esfahani, S.N., et al., 2016. Independent tuning of stiffness and toughness of additively manufactured titanium-polymer composites: simulation, fabrication, and experimental studies. *J. Mater. Process. Technol.* 238, 22–29.
- Funakubo, H., Kennedy, J.B., 1987. Shape memory alloys. Gordon and Breach, xii+ 275, 15×22 cm, Illustrated, p. 78.
- Funakubo, H., Kennedy, J., 1987. Shape memory alloys. Gordon and Breach, xii+ 275, 15×22 cm, Illustrated, p. 78.
- Frenzel, J., Zhang, Z., Somsen, C., Neuking, K., Eggeler, G., 2007. *Acta Mater.* 55, 1331–1341.
- Haberland, C., 2012. Additive Verarbeitung von NiTi- Formgedächtniswerkstoffen mittels Selective Laser Melting. Ruhr University Bochum, Aachen, Germany.
- Haberland, C., et al., 2013. Additive manufacturing of shape memory devices and pseudoelastic components. In: Proceedings of the ASME 2013 Conference on Smart Materials, Adaptive Structures and Intelligent Systems. American Society of Mechanical Engineers.
- Haberland, C., et al., 2014. On the development of high quality NiTi shape memory and pseudoelastic parts by additive manufacturing. *Smart Mater. Struct.* 23 (10), 104002.
- Haberland, C., H. Meier, J. Frenzel, 2012. On the properties of Ni-rich NiTi shape memory parts produced by selective laser melting. In: Proceedings of the ASME 2012 Conference on Smart Materials, Adaptive Structures and Intelligent Systems. American Society of Mechanical Engineers.
- Hamilton, R.F., Palmer, T.A., Bimber, B.A., 2015. Spatial characterization of the thermal-induced phase transformation throughout as-deposited additive manufactured NiTi bulk builds. *Scr. Mater.* 101, 56–59.
- Hartl, D.J., Lagoudas, D.C., 2007. Aerospace applications of shape memory alloys. *Proc. Inst. Mech. Eng., Part G: J. Aerosp. Eng.* 221 (4), 535–552.

- Imwinkelried, T., 2007. Mechanical properties of open-pore titanium foam. *J. Biomed. Mater. Res. Part A* 81 (4), 964–970.
- Itin, V., et al., 1994. Mechanical properties and shape memory of porous nitinol. *Mater. Charact.* 32 (3), 179–187.
- Kang, S.-B., et al., 2002. In vivo result of porous TiNi shape memory alloy: bone response and growth. *Mater. Trans.* 43 (5), 1045–1048.
- Karaca, H., et al., 2013. Effects of nanoprecipitation on the shape memory and material properties of an Ni-rich NiTiHF high temperature shape memory alloy. *Acta Mater.* 61 (19), 7422–7431.
- Kasperovich, G., Hausmann, J., 2015. Improvement of fatigue resistance and ductility of TiAl6V4 processed by selective laser melting. *J. Mater. Process. Technol.* 220, 202–214.
- Khoo, Z.X., et al., 2015. 3D printing of smart materials: a review on recent progresses in 4D printing. *Virtual Phys. Prototyp.* 10 (3), 103–122.
- Kienapfel, H., et al., 1999. Implant fixation by bone ingrowth. *J. Arthroplast.* 14 (3), 355–368.
- Köhl, M.B., M.; Buchkremer, H. P.; Stöver, D.; Habijan, T.; Köller, M., 2007. Powder metallurgical production, mechanical and biomedical properties of porous NiTi shape memory alloys. In: *Proceedings of the Materials and Processes for Medical Devices Conference*. Palm Desert, CA.
- Krishna, B.V., Bose, S., Bandyopadhyay, A., 2007. Fabrication and characterization of porous Ti6Al4V parts for biomedical applications using electron beam melting process. *J. Acta Biomater.* 3, 997–1006.
- Krishna, B.V., Bose, S., Bandyopadhyay, A., 2009. Fabrication of porous NiTi shape memory alloy structures using laser engineered net shaping. *J. Biomed. Mater. Res. Part B: Appl. Biomater.* 89 (2), 481–490.
- Leist, S.K., Zhou, J., 2016. Current status of 4D printing technology and the potential of light-reactive smart materials as 4D printable materials. *Virtual Phys. Prototyp.* 11 (4), 249–262.
- Li, D., 1996. Wear behaviour of TiNi shape memory alloys. *Scr. Mater.* 34 (2), 195–200.
- Lin, H., et al., 1997. Wear characteristics of TiNi shape memory alloys. *Metall. Mater. Trans. A* 28 (9), 1871–1877.
- Meier, H., et al., 2009. Selective Laser Melting of NiTi shape memory components. *Innov. Dev. Des. Manuf.: Adv. Res. Virtual Rapid Prototyp.*, 233–238.
- Melton, K., Duerig, T., 1985. Industrial applications of shape memory alloys. *Metallurgia* 52 (8), 318–319.
- Morgan, N., 2004. Medical shape memory alloy applications—the market and its products. *Mater. Sci. Eng.: A* 378 (1), 16–23.
- Oshida Yoshiki, M.S., 1991. Corrosion and biocompatibility of shape memory alloys. *Zairyo-to-Kankyo* 40 (12), 834–844.
- Ravari, M.K., et al., 2014. Numerical investigation on mechanical properties of cellular lattice structures fabricated by fused deposition modeling. *Int. J. Mech. Sci.* 88, 154–161.
- Ravari, M.K., et al., 2016. On the effects of geometry, defects, and material asymmetry on the mechanical response of shape memory alloy cellular lattice structures. *Smart Mater. Struct.* 25 (2), 025008.
- Ravari, M.K., Kadkhodaei, M., 2015. A computationally efficient modeling approach for predicting mechanical behavior of cellular lattice structures. *J. Mater. Eng. Perform.* 24 (1), 245–252.
- Ryhänen, J., et al., 1997. Biocompatibility of nickel-titanium shape memory metal and its corrosion behavior in human cell cultures. *J. Biomed. Mater. Res.* 35 (4), 451–457.
- Saedi, S., et al., 2016. Thermomechanical characterization of Ni-rich NiTi fabricated by selective laser melting. *Smart Mater. Struct.* 25 (3), 035005.
- Saedi, S., et al., 2016. The influence of heat treatment on the thermomechanical response of Ni-rich NiTi alloys manufactured by selective laser melting. *J. Alloy. Compd.* 677, 204–210.
- Saedi, S., Turabi, A.S., Andani, T.M., Haberland, C., Elahinia, M., Karaca, H., 2016. Thermo-mechanical characterization of Ni-rich NiTi shape memory alloys fabricated by selective laser melting method. *Smart Mater. Struct.*
- Shida, Y., Sugimoto, Y., 1991. Water jet erosion behaviour of Ti-Ni binary alloys. *Wear* 146 (2), 219–228.
- Shishkovsky, I., et al., 2008. Porous biocompatible implants and tissue scaffolds synthesized by selective laser sintering from Ti and NiTi. *J. Mater. Chem.* 18 (12), 1309–1317.
- Sims, S., Ayers, R., Bateman, T., 1997. Porous materials for bone engineering. In: *Materials Science Forum*. Trans Tech Publ..
- Soheil Saedi1, A.S.T., Andani2,3, Mohsen Taheri, Moghaddam2, Narges Shayesteh, Elahinia2, Mohammad, Karaca1, Haluk, 2016. Texture, aging, and superelasticity of SLM fabricated Ni-rich NiTi alloys. *Mater. Sci. Eng.: A*.
- Taheri Andani, M., 2015. Modeling, Simulation, Additive Manufacturing, and Experimental Evaluation of Solid and Porous NiTi. University of Toledo.
- Urban, R.M., et al., 1996. The bone-implant interface of femoral stems with non-circumferential porous coating. A study of specimens retrieved at autopsy\*. *J. Bone Jt. Surg.* 78 (7), 1068–1081.
- Wagner, M., J. Frenzel, G. Eggeler, 2006. Evolution of microstructural parameters during cycling of NiTi and their effect on mechanical and thermal memory. In: *SMST-2004: Proceedings of the International Conference on Shape Memory and Superelastic Technologies*. ASM International.
- Walker, J., et al., 2014. Additive manufacturing of nitinol shape memory alloys to overcome challenges in conventional nitinol fabrication. In: *Proceedings of the ASME 2014 International Mechanical Engineering Congress and Exposition*. American Society of Mechanical Engineers.
- Walker, J., M. Elahinia, C. Haberland, 2013. An investigation of process parameters on selective laser melting of nitinol. In: *Proceedings of the ASME 2013 Conference on Smart Materials, Adaptive Structures and Intelligent Systems*. American Society of Mechanical Engineers.
- Walker, J.M., et al., 2016. Process development and characterization of additively manufactured nickel–titanium shape memory parts. *J. Intell. Mater. Syst. Struct.*, [1045389X16635848].
- Wu, M.H., 2002. Fabrication of nitinol materials and components. In: *Materials Science Forum*. Trans Tech Publ..
- Wu, W., et al., 2015. Investigation on processing of ASTM A131 Eh36 high tensile strength steel using selective laser melting. *Virtual Phys. Prototyp.* 10 (4), 187–193.
- Yavari, S.A., et al., 2014. Effects of bio-functionalizing surface treatments on the mechanical behavior of open porous titanium biomaterials. *J. Mech. Behav. Biomed. Mater.* 36, 109–119.